

A CONSERVATIVE SEMI-LAGRANGIAN HYBRID HERMITE WENO SCHEME FOR LINEAR TRANSPORT EQUATIONS AND THE NONLINEAR VLASOV–POISSON SYSTEM*

NANYI ZHENG[†], XIAOFENG CAI[‡], JING-MEI QIU[§], AND JIANXIAN QIU[¶]

Abstract. In this paper, we present a high-order conservative semi-Lagrangian (SL) hybrid Hermite weighted essentially nonoscillatory (HWENO) scheme for linear transport equations and the nonlinear Vlasov–Poisson (VP) system. The proposed SL hybrid HWENO scheme adopts a weak formulation of the characteristic Galerkin method and introduces an adjoint problem for the test function in the same way as the SL discontinuous Galerkin (DG) scheme [W. Guo, R. D. Nair, and J. M. Qiu, *Monthly Weather Rev.*, 142 (2014), pp. 457–475]. Comparing with the original SL DG scheme, we introduce a hybrid moment-based HWENO reconstruction operator in space, bringing at least two benefits. Firstly, with the same order of accuracy, such a reconstruction allows lower degrees of freedom per element in the evolution process. Secondly, it naturally possesses a nonoscillatory property when dealing with discontinuity. In addition, we derive a novel troubled cell indicator which can effectively detect the discontinuous regions for the reconstruction operator. To apply the scheme for 2-D transport equations and the nonlinear VP system, we adopt a fourth-order dimensional splitting method. Positivity-preserving limiters are applied to enforce the positivity of the solution for the system having positive solutions. Finally, we show extensive numerical tests to validate the effectiveness of the proposed SL hybrid HWENO scheme.

Key words. Vlasov–Poisson system, semi-Lagrangian, mass conservation, positivity preservation, hybrid HWENO reconstruction, troubled cell indicator

AMS subject classifications. 65M60, 35L65

DOI. 10.1137/20M1363273

1. Introduction. The transport equation can be found in a variety of applications such as climate modeling and kinetic description of plasma. It can be written in the form of

$$(1.1) \quad u_t + \nabla_{\mathbf{x}} \cdot (\mathbf{a}(u, \mathbf{x}, t)u) = 0,$$

where $u(\mathbf{x}, t)$ is the scalar density function of a conserved quantity transported in a flow with velocity field $\mathbf{a}(u, \mathbf{x}, t)$ with $\mathbf{x} \in \mathbb{R}^d$. The semi-Lagrangian (SL) approach is popular for solving the transport equation. It uses fixed meshes, like the Eulerian approach, while the information propagates along the characteristics, like

*Submitted to the journal's Methods and Algorithms for Scientific Computing section August 31, 2020; accepted for publication (in revised form) June 30, 2021; published electronically October 25, 2021.

<https://doi.org/10.1137/20M1363273>

Funding: The work of the first and fourth authors was partially supported by National Natural Science Foundation (China) grant 12071392. The work of the third author was partially support by NSF grants NSF-DMS-1818924 and NSF-DMS-2111253, Air Force Office of Scientific Research FA9550-18-1-0257.

[†]School of Mathematical Sciences, Xiamen University, Xiamen, Fujian 361005, China (nyzheng@stu.xmu.edu.cn).

[‡]Department of Mathematical Sciences, University of Delaware, Newark, DE 19716 USA. Current address: Advanced Institute of Natural Sciences, Beijing Normal University at Zhuhai, Zhuhai 519087, China, and United International College (BNU-HKBU), Zhuhai 519087, China (xfcai@udel.edu, xfcai@bnu.edu.cn).

[§]Department of Mathematical Sciences, University of Delaware, Newark, DE 19716 USA (jingqiu@udel.edu).

[¶]Corresponding author. School of Mathematical Sciences and Fujian Provincial Key Laboratory of Mathematical Modeling and High-Performance Scientific Computing, Xiamen University, Xiamen, Fujian 361005, China (jxqiu@xmu.edu.cn).

the Lagrangian approach. Hence, it can escape the CFL time step restriction leading to savings in computational cost by taking larger numerical time steps, like the Lagrangian approach, while being highly accurate, like the Eulerian approach.

The SL methodology development has been coupled with the weighted essentially nonoscillatory (WENO) or discontinuous Galerkin (DG) framework [26, 24, 27, 25, 9, 16, 32, 17, 15, 20, 12, 4] with great success, yet there are pros and cons associated with each scheme. On one hand, a high-order DG method needs a high number of degrees of freedom (DOF) per element, especially in a high-dimensional setting. On the other hand, the WENO method is not as compact as the DG method, and the reconstruction function of the classical WENO method [21, 18, 29] is a rational fraction which can cause some trouble.

The Hermite WENO (HWENO) reconstruction methods were first developed in [23] and then further discussed in [30, 7, 39]. The major advantage of these HWENO methods is their compactness compared with the original WENO methods, since the first derivative or first-order moment values are adopted. For the conservation law, the schemes in [23, 30, 7, 39] only need to reconstruct nodal values at few specific spatial positions in a given cell. For those specific positions, a set of positive linear weights can be found to perform their reconstructions. Unfortunately, when the velocity field \mathbf{a} is dependent of the spatial variables, the SL formulation requires an approximated point value at any spatial position. However, the linear weights may not exist at some locations for the methods in [23, 30, 7, 39]. Hence, we adopt a new hybrid moment-based (MB) HWENO reconstruction method in [40] which takes artificial positive linear weights with their sum being one. In this paper, the hybrid MB HWENO reconstruction operator recovers a fifth-degree polynomial for each 1-D cell while [40] only gives the reconstruction formulation for specific Gauss–Legendre–Lobatto points. Theoretically, the hybrid HWENO reconstruction automatically decays to a first-degree polynomial reconstruction in the region where the solution is discontinuous. In the region where the solution is smooth, it adopts a fifth-degree polynomial reconstruction. Hence, the scheme shares a similar spirit with p -adaptive DG methods in [5, 31, 19].

The proposed SL scheme combines the weak formulation of the characteristic Galerkin method [10, 28, 15] with the hybrid MB HWENO reconstruction operator [40] for 1-D problems. Such a combination can be seen as a one-step evolution-Galerkin scheme introduced in [22] with the solution operator being the characteristic Galerkin method and the recovery operation implemented by the hybrid HWENO reconstruction operator. More recently, such a reconstruction procedure can also be explained as a P_1P_5 method as introduced in [11]. The resulting SL hybrid HWENO scheme enjoys the following benefits. Firstly, the weak formulation of Galerkin method provides a good framework to design a mass conservation scheme with ease. Secondly, compared with the SL DG method [15], it requires a lower number of DOF per element in the evolution process.

In this paper, we propose a new troubled cell indicator to hybridize an expensive nonlinear MB HWENO reconstruction operator with a linear Hermite interpolation. This new troubled cell indicator is simpler than the original KXRCF indicator adopted in [40] and performs better for our tested cases. When the analytical solution enjoys a positivity-preserving (PP) property, the PP limiter in [37] is applied to ensure the PP property of the numerical solution. Furthermore, the PP limiter can maintain the original accuracy of the proposed scheme as proved in [37]. The SL hybrid HWENO scheme is coupled with a fourth-order splitting method as in [27, 25, 15] for the 2-D linear transport equation and the nonlinear Vlasov–Poisson system. To maintain high-order accuracy in space and a low number of DOF per element for the 2-D scheme, we

apply a Lagrangian interpolation method and the Hermite interpolation method for the transformation of nodal information and modal information. From our numerical tests, we observe that the 2-D SL hybrid HWENO scheme takes roughly half the time as the 2-D P^3 SL DG scheme in [15] using the same splitting method for the same problem due to the lower number of DOF per element.

The rest of the paper is organized as follows. In section 2, we introduce the proposed scheme. The performance of the scheme is demonstrated in section 3 for linear transport equations and the nonlinear Vlasov–Poisson system. Finally, we give a conclusion in section 4.

2. The SL hybrid HWENO scheme. Since the proposed scheme is based on the framework of the P^1 SL DG scheme in [15], we will first review the P^1 SL DG scheme in subsection 2.1. Then we propose a 1-D SL hybrid HWENO scheme based on the framework in subsection 2.2. Next we extend the scheme for 2-D linear transport equation via a fourth-order dimensional splitting method in subsection 2.3; the PP limiters are discussed in subsection 2.4.

2.1. Review of the P^1 SL DG formulation. Consider a 1-D linear transport equation

$$(2.1) \quad u_t(x, t) + (a(x, t)u(x, t))_x = 0,$$

where $u(x, t)$ is the density function and $a(x, t)$ is the velocity field on $[x_L, x_R]$. We assume a discretization such that $x_L = x_{\frac{1}{2}} < x_{\frac{3}{2}} < \dots < x_{j-\frac{1}{2}} < x_{j+\frac{1}{2}} < \dots < x_{N-\frac{1}{2}} < x_{N+\frac{1}{2}} = x_R$, with $I_j := [x_{j-\frac{1}{2}}, x_{j+\frac{1}{2}}]$, $h_j := x_{j+\frac{1}{2}} - x_{j-\frac{1}{2}}$ and $x_j := (x_{j-\frac{1}{2}} + x_{j+\frac{1}{2}})/2$ for all j . In the context of HWENO scheme, we consider a DG space $V_h^1 = \{v_h : v_h|_{I_j} \in P^1(I_j) \text{ for all } j\}$, where $P^1(I_j)$ denotes the set of linear polynomials defined on I_j . We let $\Delta t^n = t^{n+1} - t^n$ and let $u^n(x) \in V_h^1$ as the numerical approximation of $u(x, t^n)$ with any given integer n .

The following locally defined adjoint problem of (2.1) is introduced: for a test function $W \in P^1(I_j)$,

$$(2.2) \quad \begin{cases} w_t + a(x, t)w_x = 0 & \text{on } [t^n, t^{n+1}), \\ w(t = t^{n+1}) = W(x). \end{cases}$$

It can be shown [15] that

$$(2.3) \quad \frac{d}{dt} \int_{I_j(t)} u(x, t)w(x, t)dx = 0,$$

where $I_j(t)$ (see Figure 1(a)) is a dynamic interval whose boundaries are characteristics passing through $x_{j\pm\frac{1}{2}}$ at $t = t^{n+1}$. Equation (2.3) naturally leads to the following scheme:

$$(2.4) \quad \int_{I_j} u^{n+1}W dx = \int_{I_j^*} u(x, t^n)w(x, t^n)dx,$$

where $I_j^* = [x_{j-\frac{1}{2}}^*, x_{j+\frac{1}{2}}^*]$ and $x_{j\pm\frac{1}{2}}^*$ are the feet of characteristics passing through $(x_{j\pm\frac{1}{2}}, t^{n+1})$ at t^n .

To update u^{n+1} on I_j , one has to properly evaluate the right-hand side of (2.4) which is summarized as follows.

1. Trace characteristics backward.

We solve a final value ordinary differential equation (ODE) problem,

$$(2.5) \quad \frac{dX(t)}{dt} = a(X(t), t),$$

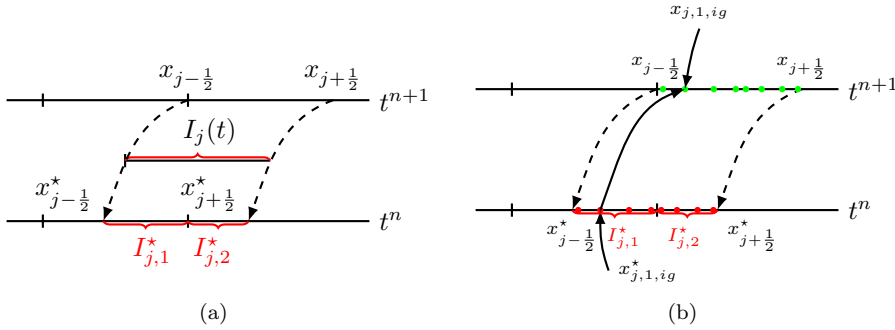


FIG. 1. Schematic illustration for the proposed scheme in 1-D case.

with final values $X(t^{n+1}) = x_{j\pm\frac{1}{2}}$ to obtain $x_{j\pm\frac{1}{2}}^*$. This can be numerically solved by a high-order Runge–Kutta method. We define $\cup I_{j,l}^* = I_j^*$ such that each subinterval is bounded by grid points or $x_{j\pm\frac{1}{2}}^*$. See Figure 1(a) as an example where I_j^* is divided into two subintervals: $I_{j,1}^* = [x_{j-1/2}^*, x_{j-1/2}]$ and $I_{j,2}^* = [x_{j-1/2}, x_{j+1/2}^*]$. Then, as shown in Figure 1(b), we locate 4 Gauss–Legendre (GL) points $\{x_{j,l,ig}^*\}_{ig=1}^4$ in each subinterval.

2. Approximate test function $w(x, t^n)$.

We solve the ODE (2.5) with an initial value $X(t^n) = x_{j,l,ig}^*$ to locate $x_{j,l,ig}$ at $t = t^{n+1}$ (see Figure 1(b)). Then, by the adjoint problem (2.2), we have

$$(2.6) \quad w(x_{j,l,ig}^*, t^n) = W(x_{j,l,ig}).$$

3. Update of the solution at $t = t^{n+1}$.

Given $W(x) = 1$ and $(x - x_j)/h_j$, respectively,

$$(2.7) \quad \begin{aligned} \frac{1}{h_j} \int_{I_j} u(x, t^{n+1}) W(x) dx &= \frac{1}{h_j} \sum_l \int_{I_{j,l}^*} u(x, t^n) w(x, t^n) dx \\ &\approx \frac{1}{h_j} \sum_l \sum_{ig} u(x_{j,l,ig}^*, t^n) w(x_{j,l,ig}^*, t^n) \omega_{ig}^{GL} \frac{|I_{j,l}^*|}{2} \\ &= \frac{1}{h_j} \sum_l \sum_{ig} u(x_{j,l,ig}^*, t^n) W(x_{j,l,ig}) \omega_{ig}^{GL} \frac{|I_{j,l}^*|}{2}, \end{aligned}$$

where $\{\omega_{ig}^{GL}\}$ are the four GL weights and $|\cdot|$ represents the length of a given interval. Denoting the approximations for the first two moments of the solution at t^n by \bar{u}_j^n and \bar{v}_j^n , then

$$(2.8) \quad u^n(x) = \bar{u}_j^n + 12\bar{v}_j^n \left(\frac{x - x_j}{h_j} \right), \quad x \in I_j \quad \forall j, \quad \forall n.$$

The P^1 SL DG scheme is

$$(2.9) \quad \bar{u}_j^{n+1} = \frac{1}{h_j} \sum_l \sum_{ig} u^n(x_{j,l,ig}^*) \omega_{ig}^{GL} \frac{|I_{j,l}^*|}{2},$$

$$(2.10) \quad \bar{v}_j^{n+1} = \frac{1}{h_j} \sum_l \sum_{ig} u^n(x_{j,l,ig}^*) \left(\frac{x_{j,l,ig} - x_j}{h} \right) \omega_{ig}^{GL} \frac{|I_{j,l}^*|}{2}.$$

Remark 2.1. (2.9) and (2.10) represent the 1-D P^1 SL DG formulation in [15] except that we adopt the 4-point GL quadrature rather than the 2-point Gauss–Legendre–Lobatto quadrature. The 4-point GL quadrature offers an eighth-order sufficiently high-order accuracy in the HWENO P_1P_5 reconstruction framework.

2.2. Hybrid HWENO reconstruction operator. With the SL MB method introduced above, we introduce the hybrid MB HWENO reconstruction operator to establish the 1-D SL hybrid HWENO scheme via the P_1P_5 framework [11] in this subsection. We take the solution space and test function space to be V_h^1 in our scheme. However, another set of piecewise polynomials of degree 5 based on the same grid, denoted as V_h^5 , undertakes the work of solution evaluation in the time evolution.

In particular, the SL hybrid HWENO scheme takes

$$(2.11) \quad \bar{u}_j^{n+1} = \frac{1}{h_j} \sum_l \sum_{ig} H^n(x_{j,l,ig}^*) \omega_{ig}^{GL} \frac{|I_{j,l}^*|}{2},$$

$$(2.12) \quad \bar{v}_j^{n+1} = \frac{1}{h_j} \sum_l \sum_{ig} H^n(x_{j,l,ig}^*) \left(\frac{x_{j,l,ig} - x_j}{h} \right) \omega_{ig}^{GL} \frac{|I_{j,l}^*|}{2}$$

in (2.9) and (2.10), where $H^n(x) \in V_h^5$ is constructed based on $u^n(x)$ by the hybrid MB HWENO reconstruction operator.

Below we will describe the hybrid HWENO reconstruction procedure in constructing $H^n(x)$, which is in the same spirit as in [40]. Again, we want to emphasize that the new hybrid HWENO reconstruction method can build a single polynomial $H^n(x)$ on each computational cell, while those in [23, 30, 7, 39] are only designed to reconstruct point values at specific spatial positions. For convenience, we assume that a uniform mesh is applied, i.e., $h_j \equiv h$ for all j . We define $\xi_j(x) = (x - x_j)/h$ and a group of local orthogonal bases of $P^5(I_j)$ denoted as $\{v^{(\alpha)}(\xi_j)\}_{\alpha=0}^5$ with

$$(2.13) \quad \left\{ \begin{aligned} v^{(0)} &= 1; & v^{(1)} &= \xi_j; & v^{(2)} &= \xi_j v^{(1)} - \frac{1}{12} v^{(0)}; & v^{(3)} &= \xi_j v^{(2)} - \frac{1}{15} v^{(1)}; \\ v^{(4)} &= \xi_j v^{(3)} - \frac{9}{140} v^{(2)}; & v^{(5)} &= \xi_j v^{(4)} - \frac{4}{63} v^{(3)} \end{aligned} \right\}.$$

The hybrid HWENO reconstruction operator is summarized as follows.

Step 1. Identify the troubled cell, and modify the first-order moment in the troubled cell. We detect the smoothness of the numerical solution in a given cell, say I_j , by the new troubled cell indicator $\mathcal{I}(\bar{u}_{j-1}^n, \bar{u}_j^n, \bar{u}_{j+1}^n, \bar{v}_j^n)$:

1. Construct three linear polynomials $\{p_l(x)\}$ satisfying

$$(2.14) \quad \begin{aligned} \frac{1}{h} \int_{I_j} p_1(x) dx &= \bar{u}_j^n, \quad \text{and} \quad \frac{1}{h} \int_{I_j} p_1(x) \left(\frac{x - x_j}{h} \right) dx = \bar{v}_j^n; \\ \frac{1}{h} \int_{I_{j+l}} p_2(x) dx &= \bar{u}_{j+l}^n, \quad l = -1, 0; \quad \frac{1}{h} \int_{I_{j+l}} p_3(x) dx = \bar{u}_{j+l}^n, \quad l = 0, 1. \end{aligned}$$

2. Compute the smoothness indicators $\{\beta_l\}$ [21, 18, 29] of $\{p_l(x)\}$:

$$(2.15) \quad \beta_1 = 144 (\bar{v}_j^n)^2, \quad \beta_2 = (\bar{u}_{j-1}^n - \bar{u}_j^n)^2, \quad \beta_3 = (\bar{u}_j^n - \bar{u}_{j+1}^n)^2.$$

3. Calculate a new parameter as in [41]:

$$(2.16) \quad \tau = \left(\frac{|\beta_1 - \beta_2| + |\beta_1 - \beta_3|}{2} \right)^2.$$

4. The new troubled cell indicator is obtained by

$$(2.17) \quad \mathcal{I}(\bar{u}_{j-1}^n, \bar{u}_j^n, \bar{u}_{j+1}^n, \bar{v}_j^n) = \begin{cases} 1, & \tau > c_1 h^{c_2} \max\{\beta_1, \beta_2, \beta_3\}, \\ 0 & \text{otherwise.} \end{cases}$$

The principle (2.17) is based on the fact that

$$(2.18) \quad \tau = \left((u''(x_j))^2 h^4 \right) \beta_l + O(h^7), \quad l = 1, 2, 3,$$

in a smooth region. Here, c_1 and c_2 are two parameters determining the sensitivity of the indicator. The smaller $c_1 h^{c_2}$ is, the more troubled cells are found for a given problem. By (2.18), we know that $c_1 h^{c_2}$ should be larger than h^4 and smaller than 1. We found that a range of $[h^3, h^2]$ is more suitable for $c_1 h^{c_2}$ via extensive tests. In section 3, we choose $c_1 = 0.2$ and $c_2 = 2$.

If the cell I_j is identified as a troubled cell, we modify the first-order moment \bar{v}_j^n by the HWENO reconstruction operator \mathcal{H}_j^{W1} as in [40]:

1. Calculate the first-order moments, denoted as $\{\tilde{v}_{j,l}^n\}$, of a fourth-degree polynomial $q_1(x)$ and two linear polynomials $\{q_l(x)\}_{l=2}^3 := \{p_l(x)\}_{l=2}^3$:

$$(2.19) \quad \begin{aligned} \tilde{v}_{j,1}^n &= \frac{-5\bar{u}_{j-1}^n + 5\bar{u}_{j+1}^n - 22\bar{v}_{j-1}^n - 22\bar{v}_{j+1}^n}{76}, \\ \tilde{v}_{j,2}^n &= \frac{-\bar{u}_{j-1}^n + \bar{u}_j^n}{12}, \quad \tilde{v}_{j,3}^n = \frac{-\bar{u}_j^n + \bar{u}_{j+1}^n}{12}, \end{aligned}$$

where $q_1(x)$ is constructed based on

$$(2.20) \quad \begin{aligned} \frac{1}{h} \int_{I_{j+l}} q_1(x) dx &= \bar{u}_{j+l}^n, \quad l = -1, 0, 1; \\ \frac{1}{h} \int_{I_{j+l}} q_1(x) \left(\frac{x - x_{j+l}}{h} \right) dx &= \bar{v}_{j+l}^n, \quad l = -1, 1. \end{aligned}$$

2. Choose a group of positive linear weights $\{\gamma_l\}$ such that the sum of them is one. In this paper, $\{\gamma_l\} = \{0.98, 0.01, 0.01\}$ is used. Calculate the nonlinear weights of $\{q_l(x)\}$ as $\{\omega_l\}$ as shown in Appendix B.
3. Reconstruct the first-order moment:

$$(2.21) \quad \tilde{v}_j^n = \mathcal{H}_j^{W1}(\bar{u}_{j-1}^n, \bar{u}_j^n, \bar{u}_{j+1}^n, \bar{v}_{j-1}^n, \bar{v}_{j+1}^n) = \omega_1 \left(\frac{1}{\gamma_1} \tilde{v}_{j,1}^n - \sum_{l=2}^3 \frac{\gamma_l}{\gamma_1} \tilde{v}_{j,l}^n \right) + \sum_{l=2}^3 \omega_l \tilde{v}_{j,l}^n.$$

For a good cell, say I_j , we also use the new notation $\tilde{v}_j^n = \bar{v}_j^n$. Then, we obtain a new set of first-order moments $\{\tilde{v}_j^n\}$, which is useful for better understanding of the hybrid MB HWENO reconstruction as shown below.

Step 2. Build the reconstructed $H^n(x)$ in V_h^5 .

We perform different reconstruction methods based on the troubled cell indicator, i.e.,

$$(2.22) \quad \begin{aligned} H^n|_{I_j}(x) &= (1 - \mathcal{I}_j) \mathcal{H}_j(\bar{u}_{j-1}^n, \bar{u}_j^n, \bar{u}_{j+1}^n, \bar{v}_{j-1}^n, \bar{v}_j^n, \bar{v}_{j+1}^n) \\ &\quad + \mathcal{I}_j \mathcal{H}_j^{W_2}(\bar{u}_{j-1}^n, \bar{u}_j^n, \bar{u}_{j+1}^n, \tilde{v}_{j-1}^n, \tilde{v}_j^n, \tilde{v}_{j+1}^n), \end{aligned}$$

where $\mathcal{I}_j = \mathcal{I}(\bar{u}_{j-1}^n, \bar{u}_j^n, \bar{u}_{j+1}^n, \bar{v}_j^n)$, \mathcal{H}_j is the linear Hermite interpolation operator, and $\mathcal{H}_j^{W_2}$ is the HWENO reconstruction operator which gives a reconstruction polynomial.

We define the linear Hermite interpolation operator \mathcal{H}_j [40] as follows:

$$(2.23) \quad \mathcal{H}_j(\bar{u}_{j-1}^n, \bar{u}_j^n, \bar{u}_{j+1}^n, \tilde{v}_{j-1}^n, \tilde{v}_j^n, \tilde{v}_{j+1}^n) = \sum_{k=0}^5 a_k v^{(k)}(\xi_j(x)),$$

where the coefficients $\{a_k\}$ are obtained based on the following conditions:

$$(2.24) \quad \begin{aligned} \frac{1}{h} \int_{I_{j+l}} \mathcal{H}_j(\bar{u}_{j-1}^n, \bar{u}_j^n, \bar{u}_{j+1}^n, \tilde{v}_{j-1}^n, \tilde{v}_j^n, \tilde{v}_{j+1}^n) dx &= \bar{u}_{j+l}^n, \quad l = -1, 0, 1, \\ \frac{1}{h} \int_{I_{j+l}} \mathcal{H}_j(\bar{u}_{j-1}^n, \bar{u}_j^n, \bar{u}_{j+1}^n, \tilde{v}_{j-1}^n, \tilde{v}_j^n, \tilde{v}_{j+1}^n) \left(\frac{x - x_{j+l}}{h} \right) dx &= \tilde{v}_{j+l}^n, \quad l = -1, 0, 1. \end{aligned}$$

Noticing that [40] only gives the reconstruction formula at specific Gauss–Legendre–Lobatto points, we will present the explicit expression of $\mathcal{H}_j^{W_2}$ as a polynomial below:

1. Construct a fifth-degree polynomial, denoted by $Q_1(x)$, on a big stencil $\mathcal{T}_1 = \{I_{j-1}, I_j, I_{j+1}\}$ satisfying

$$(2.25) \quad Q_1(x) = \mathcal{H}_j(\bar{u}_{j-1}^n, \bar{u}_j^n, \bar{u}_{j+1}^n, \tilde{v}_{j-1}^n, \tilde{v}_j^n, \tilde{v}_{j+1}^n) := \sum_{k=0}^5 a_k v^{(\alpha)}(\xi_j(x)), \quad x \in I_j.$$

2. Construct two quadratic polynomials, denoted by $Q_2(x)$ and $Q_3(x)$, on two small stencils $\mathcal{T}_2 = \{I_{j-1}, I_j\}$ and $\mathcal{T}_3 = \{I_j, I_{j+1}\}$ satisfying

$$(2.26) \quad \begin{aligned} \frac{1}{h} \int_{I_{j+l}} Q_2(x) dx &= \bar{u}_{j+l}^n, \quad l = -1, 0, \quad \frac{1}{h} \int_{I_j} Q_2(x) \left(\frac{x - x_j}{h} \right) dx = \tilde{v}_j^n; \\ \frac{1}{h} \int_{I_{j+l}} Q_3(x) dx &= \bar{u}_{j+l}^n, \quad l = 0, 1, \quad \frac{1}{h} \int_{I_j} Q_3(x) \left(\frac{x - x_j}{h} \right) dx = \tilde{v}_j^n. \end{aligned}$$

The explicit expressions of $\{Q_l\}_{l=2}^3$ are

$$(2.27) \quad Q_l(x) = \sum_{k=0}^1 a_k v^{(k)}(\xi_j(x)) + a_{l,2} v^{(2)}(\xi_j(x)), \quad l = 2, 3,$$

where $a_0 = \bar{u}_j^n$, $a_1 = 12\tilde{v}_j^n$.

3. Choose a group of positive linear weights $\{\tilde{\gamma}_l\}$ such that the sum of them is one. In this paper, $\{\tilde{\gamma}_l\} = \{0.98, 0.01, 0.01\}$ is used. Calculate the nonlinear weights of $\{Q_l\}$ as $\{\tilde{\omega}_l\}$ as shown in Appendix B.

4. Perform the reconstruction by the following expression:

$$\begin{aligned}
 (2.28) \quad & \mathcal{H}_i^{W2}(\bar{u}_{j-1}^n, \bar{u}_j^n, \bar{u}_{j+1}^n, \bar{v}_{j-1}^n, \bar{v}_j^n, \bar{v}_{j+1}^n) \\
 &= \tilde{\omega}_1 \left(\frac{1}{\tilde{\gamma}_1} Q_1(x) - \sum_{l=2}^3 \frac{\tilde{\gamma}_l}{\tilde{\gamma}_1} Q_l(x) \right) + \sum_{l=2}^3 \tilde{\omega}_l Q_l(x) \\
 &= a_0 + a_1 v^{(1)}(\xi_j(x)) + \left[\tilde{\omega}_1 \frac{1}{\tilde{\gamma}_1} a_2 + \sum_{l=2}^3 \left(\tilde{\omega}_l - \tilde{\omega}_1 \frac{\tilde{\gamma}_l}{\tilde{\gamma}_1} \right) a_{l,2} \right] v^{(2)}(\xi_j(x)) \\
 &\quad + \sum_{k=3}^5 \frac{\tilde{\omega}_1}{\tilde{\gamma}_1} a_k v^{(k)}(\xi_j(x)).
 \end{aligned}$$

Below, we give some basic propositions of the proposed 1-D scheme.

PROPOSITION 2.2. *The 1-D SL hybrid HWENO scheme (2.11)–(2.12) is mass conservative if periodic boundary condition is imposed.*

Proof.

$$\begin{aligned}
 (2.29) \quad & h \sum_{j=1}^N \bar{u}_j^{n+1} = \sum_{j=1}^N \left(\sum_l \sum_{ig} H^n(x_{j,l,ig}^*) \omega_{ig}^{GL} \frac{|I_{j,l}^*|}{2} \right) = \sum_{j=1}^N \int_{I_j^*} H^n(x) dx \\
 &= \sum_{j=1}^N \int_{I_j} H^n(x) dx = h \sum_{j=1}^N \bar{u}_j^n,
 \end{aligned}$$

where the second equality is based on the fact that 4-point GL quadrature is exact for fifth-degree polynomials, the third equality comes from the periodic boundary condition, and the last equality comes from the property of the hybrid MB HWENO reconstruction operator. \square

If we set $H^n|_{I_j} = \mathcal{H}_j(\bar{u}_{j-1}^n, \bar{u}_j^n, \bar{u}_{j+1}^n, \bar{v}_{j-1}^n, \bar{v}_j^n, \bar{v}_{j+1}^n)$ for all j , which means that we use the linear Hermite interpolation operator for all cells, we call the numerical update (2.11)–(2.12) an *SL Hermite scheme*.

PROPOSITION 2.3 (L^2 stability). *The numerical update given by (2.11)–(2.12) is unconditionally stable for transport equations with constant coefficients and periodic boundary condition if $H^n(x)$ is constructed by the linear Hermite interpolation.*

Proof. We give the proof in Appendix C for the sake of the conciseness. \square

2.3. Dimensional splitting. In this subsection, we introduce how to couple the 1-D SL hybrid HWENO scheme with the fourth-order dimensional splitting method. The transport equation (1.1) in 2-D case can be split into two 1-D transport equations:

$$(2.30) \quad u_t + (a(x, y, t)u)_x = 0,$$

$$(2.31) \quad u_t + (b(x, y, t)u)_y = 0.$$

With the two split 1-D subproblems, we adopt the fourth-order dimensional splitting technique developed by Forest and Ruth [14] and by Yoshida [33, 34] summarized as (A.1) in Appendix A.

In order to perform the dimensional splitting, we apply a similar framework as [25]. Since the 1-D SL hybrid HWENO scheme obtains a solution in V_h^1 , directly

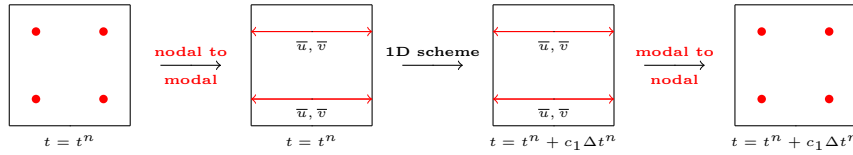


FIG. 2. Schematic illustration of the 2-D scheme for stage 1 of (A.1).

transforming the nodal and the modal information as in [25] can only give second-order nodal information. Hence, we introduce high-order reconstructions shown in Algorithms 2.1 and 2.2 to transform the nodal and the modal information. We find that the high-order interchange of the nodal and the modal information is the key to preserve the high-order accuracy in space and low number of DOF per 2-D element at the same time. We briefly summarize the proposed 2-D SL hybrid HWENO scheme as follows.

Assume a 2-D Cartesian mesh on $\Omega := I^x \times I^y := [x_L, x_R] \times [y_L, y_R]$ by defining two uniform 1-D meshes $\{x_{i+\frac{1}{2}}\}_{i=0}^{N_x}$ and $\{y_{j+\frac{1}{2}}\}_{j=0}^{N_y}$ similar to the one in section 2.1 with $I_i^x := [x_{i-\frac{1}{2}}, x_{i+\frac{1}{2}}]$, $I_j^y := [y_{j-\frac{1}{2}}, y_{j+\frac{1}{2}}]$, $h_x \equiv x_{i+\frac{1}{2}} - x_{i-\frac{1}{2}}$, $h_y \equiv y_{j+\frac{1}{2}} - y_{j-\frac{1}{2}}$, and $I_{ij} := I_i^x \times I_j^y$ for $i = 1, 2, \dots, N_x, j = 1, 2, \dots, N_y$. Then, within any given rectangular cell I_{ij} , we locate 2 GL points in both directions as (x_{ig}^i, y_{jg}^j) for $ig, jg = 1, 2$ (see Figure 2). Based on the 2-D mesh defined above, we take our solution space to be 4 point values at GL points per element, which is equivalent to $V_h^{2D} = \{v_h : v_h|_{I_{ij}} \in Q^1(I_{ij}) \text{ for all } i, j\}$. Further, we assume that our 2-D scheme obtains $\{u^{(k),n}\}_{k=1}^6 \subseteq V_h^{2D}$ and $u^{n+1} \in V_h^{2D}$ in each stage of (A.1). The proposed 2-D scheme for stage 1 of (A.1) is implemented as follows:

1. For each y_{jg}^j , we use $\{u^n(x_{ig}^i, y_{jg}^j)\}_{l=i-1, ig=1}^{i+1, 2}$ to obtain the Lagrangian interpolation polynomial $P_i(x)$ for all i . Then we take $\{\frac{1}{h_x} \int_{I_i} P_i(x) dx\} := \{\bar{u}_i^{j,jg}\}$ and $\{\frac{1}{h_x} \int_{I_i} P_i(x)(x - x_i)/h_x dx\} := \{\bar{v}_i^{j,jg}\}$ as the initial condition of the 1-D scheme (see Algorithm 2.1).
2. Evolve (2.30) for $c_1 \Delta t^n$ by the 1-D SL hybrid HWENO scheme and obtain the new modal information $\{\bar{u}_i^{new,j,jg}\}$ and $\{\bar{v}_i^{new,j,jg}\}$ at $t^n + c_1 \Delta t^n$.
3. For each y_{jg}^j , we use $\{\bar{u}_l^{new,j,jg}\}_{l=i-1}^{i+1}$ and $\{\bar{v}_l^{new,j,jg}\}_{l=i-1}^{i+1}$ to obtain the Hermite interpolation $H_i(x)$ for all i . Then we set $u^{(1),n}(x_{ig}^i, y_{jg}^j) = H_i(x_{ig}^i)$ for all i, ig (see Algorithm 2.2).

Then, the proposed 2-D SL hybrid MB HWENO scheme takes similar procedures above for each stage in (A.1), and the numerical solution u^{n+1} is updated.

We use linear reconstructions in Algorithms 2.1 and 2.2 rather than WENO-type reconstructions due to the following reasons: firstly, it is hard to maintain the mass conservation property when adopting WENO-type reconstructions since the 2-D mass conservation in our framework relies on a special symmetry of the coefficients $\{c_{ig}^l\}$, $\{c_l^{\bar{u}}\}$, $\{c_l^{\bar{v}}\}$, $\{d_l^{\bar{u}}\}$, and $\{d_l^{\bar{v}}\}$ in (2.33), and (2.35) while WENO-type reconstructions destroy the symmetry; secondly, the reconstructions in Algorithms 2.1 and 2.2 are only used for transforming spatial information rather than evolving the solution in time; thirdly, WENO-type reconstructions are costly. In practice, numerical oscillation is still well controlled according to our observations.

In the dimensional splitting setting, the SL Hermite-type scheme has a lower number of DOF per cell and thus lower computational cost. For example, in the

Algorithm 2.1. Reconstruction in transforming nodal information to modal information.

1. Construct a Lagrangian interpolation polynomial $\{P_i(x)\}$ satisfying

$$(2.32) \quad P_i(x_{ig}^l) = u^n(x_{ig}^l, y_{jg}^j), \quad l = i - 1, i, i + 1, \quad ig = 1, 2.$$

2. Compute the first two moments of $P_i(x)$:

$$(2.33) \quad \begin{aligned} \frac{1}{h_x} \int_{I_i} P_i(x) dx &= \sum_{l=i-1, ig=1}^{i+1, 2} c_{ig}^l u^n(x_{ig}^l, y_{jg}^j) := \bar{u}_i^{j,jg}, \\ \frac{1}{h_x} \int_{I_i} P_i(x)(x - x_i)/h_x dx &= \sum_{l=i-1, ig=1}^{i+1, 2} d_{ig}^l u^n(x_{ig}^l, y_{jg}^j) := \bar{v}_i^{j,jg}, \end{aligned}$$

where $\{c_{ig}^l\}$, and $\{d_{ig}^l\}$ are constant coefficients independent of i .

Algorithm 2.2. Reconstruction in transforming modal information to nodal information.

1. Construct a Hermite interpolation polynomial $\{H_i(x)\}$ satisfying

$$(2.34) \quad H_i(x) = \mathcal{H}_i(\bar{u}_i^{new,j,jg}, \bar{u}_i^{new,j,jg}, \bar{u}_{i+1}^{new,j,jg}, \bar{v}_i^{new,j,jg}, \bar{v}_i^{new,j,jg}, \bar{v}_{i+1}^{new,j,jg}).$$

2. Compute $\{H_i(x_{ig}^i)\}$:

$$(2.35) \quad \begin{aligned} H_i(x_1^i) &= \sum_{l=i-1}^{i+1} \bar{c}_l^i \bar{u}_l^{new,j,jg} + \sum_{l=i-1}^{i+1} \bar{c}_l^i \bar{v}_l^{new,j,jg}, \\ H_i(x_2^i) &= \sum_{l=i-1}^{i+1} \bar{d}_l^i \bar{u}_l^{new,j,jg} + \sum_{l=i-1}^{i+1} \bar{d}_l^i \bar{v}_l^{new,j,jg}, \end{aligned}$$

where $\{\bar{c}_l^i\}$, $\{\bar{c}_l^i\}$, $\{\bar{d}_l^i\}$, and $\{\bar{d}_l^i\}$ are constant coefficients independent of i .

dimensional splitting setting, 2 nodal points per direction per cell are needed for the SL hybrid HWENO scheme (see Figure 2), while 4 nodal points are needed for the P^3 SL DG scheme. Hence, for 2-D problems, if $N_x = N_y = N$, the SL hybrid HWENO scheme takes $7 \times (2N) = 14N$ 1-D solvers per time step while the P^3 SL DG scheme needs $7 \times (4N) = 28N$ 1-D solvers. For 3-D problems, we can estimate that the fourth-order splitting method requires 25 stages per time step. Hence, the SL hybrid HWENO scheme takes $25 \times (2N) \times (2N) = 100N^2$ 1-D solvers per time step while the SL P^3 SL DG scheme takes $25 \times (4N) \times (4N) = 400N^2$ 1-D solvers. The lower number of DOF per dimension is of great importance for high-dimensional problems under the dimensional splitting setting.

Below, we provide the proof of the 2-D mass conservation property.

PROPOSITION 2.4. *The 2-D SL hybrid HWENO scheme is mass conservative if periodic boundary condition is imposed.*

Proof. With periodic boundary condition and the special symmetry of the coefficients $\{c_{ig}^l\}$, $\{c_l^i\}$, $\{c_l^i\}$, $\{d_l^i\}$, and $\{d_l^i\}$, one can easily verify that

$$(2.36) \quad \begin{aligned} h_x \sum_{i=1}^{N_x} \bar{u}_i^{j,jg} &= h_x \sum_{i=1}^{N_x} \left(\frac{u^n(x_1^i, y_{jg}^j) + u^n(x_2^i, y_{jg}^j)}{2} \right), \\ h_x \sum_{i=1}^{N_x} \bar{u}_i^{new,j,jg} &= h_x \sum_{i=1}^{N_x} \left(\frac{H_i(x_1^i) + H_i(x_2^i)}{2} \right) \end{aligned}$$

in Algorithms 2.1 and 2.2.

Since the 1-D scheme is mass conservative, we have

$$(2.37) \quad h_x \sum_{i=1}^{N_x} \bar{u}_i^{j,jg} = h_x \sum_{i=1}^{N_x} \bar{u}_i^{new,j,jg}.$$

Comparing (2.36)–(2.37), we have

$$(2.38) \quad h_x \sum_{i=1}^{N_x} \left(\frac{u^n(x_1^i, y_{jg}^j) + u^n(x_2^i, y_{jg}^j)}{2} \right) = h_x \sum_{i=1}^{N_x} \left(\frac{u^{(1),n}(x_1^i, y_{jg}^j) + u^{(1),n}(x_2^i, y_{jg}^j)}{2} \right).$$

Notice that the indexes j and jg are arbitrary; we have

$$(2.39) \quad \begin{aligned} h_x h_y \sum_{i=1, j=1}^{N_x, N_y} \left(\frac{u^n(x_1^i, y_1^j) + u^n(x_2^i, y_1^j) + u^n(x_1^i, y_2^j) + u^n(x_2^i, y_2^j)}{4} \right) \\ = h_x h_y \sum_{i=1, j=1}^{N_x, N_y} \left(\frac{u^{(1),n}(x_1^i, y_1^j) + u^{(1),n}(x_2^i, y_1^j) + u^{(1),n}(x_1^i, y_2^j) + u^{(1),n}(x_2^i, y_2^j)}{4} \right). \end{aligned}$$

Following similar procedures for the other stages, we finish the proof. \square

2.4. PP limiter. In this subsection, we introduce the PP limiter in [37] to ensure the PP property of the numerical solution when the relevant property is enjoyed by the exact solution. In the earlier works [25, 38, 15], another type of PP limiter introduced in [35, 36] is adopted. Such a PP limiter as in [35, 36] would require the minimum value of $H^n(x)$ in each cell in our framework. However, it is impossible to obtain the extreme points of a piecewise fifth-degree polynomial $H^n(x)$ theoretically. Hence, we apply the new PP limiter introduced in [37], which only requires the minimum value of $H^n(x)$ at the GL points we defined in section 2.1 at each cell.

To explain how the PP limiter is applied in our scheme, we denote the subintervals defined in step 1 of subsection 2.1 within a given cell I_j by $\{I_{j,l}\}$. Then, denote the local GL points within $I_{j,l}$ by $\{\tilde{x}_{j,l,ig}\}$. The PP limiter [37] replaces the $H^n(x)$ in (2.22) with

$$(2.40) \quad \tilde{H}^n(x) = \theta (H^n(x) - \bar{u}_j^n) + \bar{u}_j^n, \quad x \in I_j,$$

where

$$(2.41) \quad \theta = \min \left\{ \left| \frac{\bar{u}_j^n}{m_j - \bar{u}_j^n} \right|, 1 \right\}, \quad m_j = \min_{l,ig} \{H^n(\tilde{x}_{j,l,ig})\}.$$

It can be proved as in [37] that

$$(2.42) \quad \{\tilde{H}^n(\tilde{x}_{j,l,ig})\} \subset [0, +\infty) \text{ if } \bar{u}_j^n \in [0, +\infty) \quad \forall l, ig.$$

Furthermore, it was proved in [37] that $\tilde{H}^n(x)$ can still maintain the accuracy of $H^n(x)$ approximating $u(x, t^n)$. Applying this PP limiter, the PP of cell average of the 1-D SL hybrid HWENO scheme is easily obtained by (2.11) and (2.42).

Notice that $\{u^n(x_{ig}^l, y_{jg}^j)\}_{l=i-1, ig=1}^{i+1}$ does not guarantee $\bar{u}_i^{j,jg} \geq 0$ in Algorithm 2.1 and $\{\bar{u}_l^{new,j,jg}\}_{l=i-1}^{i+1} \subset [0, +\infty)$ does not guarantee $\{H_i(x_{ig}^i)\}_{ig=1}^2 \subset [0, +\infty)$ in Algorithm 2.2. Hence, we need extra PP limiters applying on Algorithms 2.1 and 2.2 if $u(x, y, 0) \geq 0$ for the 2-D SL hybrid HWENO scheme. For the compactness of the paper, we summarize the PP limiters for Algorithm 2.1 and Algorithm 2.2 as Algorithms D.1 and D.2 as shown in Appendix D.

PROPOSITION 2.5. *The new PP limiters (Algorithms D.1 and D.2) enjoy the following three properties:*

1. *the corresponding cell averages or nodal values are strictly enforced to be nonnegative;*
2. *they are sixth-order accurate limiters;*
3. *the mass conservation property is not destroyed.*

Proof. We skip the proof since it is nearly the same as the one in [37]. □

3. Numerical tests.

3.1. Numerical tests for linear transport equations. In this subsection, we test three classical 2-D linear cases: transport equation with constant coefficients, rigid body rotation, and swirling deformation flow. Through these three cases, we investigate the following properties of our schemes:

1. spatial and temporal order of accuracy,
2. computational efficiency,
3. effectiveness of the new troubled cell indicator,
4. essentially nonoscillatory property.

Unless otherwise specified, we take $\Delta t = \frac{\text{CFL}}{\max\{\frac{|a(x,y,t)|}{h_x}\} + \max\{\frac{|b(x,y,t)|}{h_y}\}}$ and $\text{CFL} =$

10.2. The L^2 error of the numerical solution is calculated by the following formula:

$$(3.1) \quad \begin{aligned} & \|u(\cdot, \cdot, T) - u^*(\cdot, \cdot)\|_2 \\ & := \sqrt{\frac{1}{|\Omega|} \sum_{i=1}^{N_x} \sum_{j=1}^{N_y} \frac{h_x h_y}{4} \sum_{ig=1}^2 \sum_{jg=1}^2 \left(u(x_{ig}^i, y_{jg}^j, T) - u^*(x_{ig}^i, y_{jg}^j)\right)^2}, \end{aligned}$$

where u^* represents a numerical solution and $|\Omega|$ is the area of the computational domain Ω . The numerical solutions in the figures below are plotted based on the cell averages of the numerical solutions. The PP limiters are applied in the cases where the initial conditions are positive. The P^3 SL DG scheme shown below presents the one constructed in [15].

Example 3.1 (2-D transport equation with constant coefficients). Consider

$$(3.2) \quad u_t + u_x + u_y = 0, \quad x \in [-\pi, \pi], \quad y \in [-\pi, \pi].$$

We solve (3.2) with a smooth initial data $u(x, y, 0) = \sin(x + y)$. The exact solution for this problem is $u(x, y, t) = \sin(x + y - 2t)$.

Since there is no dimensional splitting error in time for (3.2), the spatial error is dominant. Thus, this example can test the spatial order of accuracy of the 2-D schemes. And we only take the simplest first-order dimensional splitting, which first evolves Δt^n for (2.30) and then evolves (2.31) for Δt^n for each time step. Table 1 shows the L^2 errors, corresponding order of accuracy, and corresponding CPU times of the SL Hermite scheme, the SL hybrid HWENO scheme, and the P^3 SL DG scheme at $T = 2$. The meshes of $\{40 \times 40, 80 \times 80, 160 \times 160, 320 \times 320\}$ are applied. As shown, the errors of the former two schemes are the same for all meshes, which means that all cells are identified as good cells by the indicator for this test. As expected, the spatial orders of the former two schemes are sixth while the spatial order of the P^3 SL DG scheme is fourth. We also observe that the CPU times of the former two schemes are roughly half those of the P^3 SL DG scheme for the same mesh. This is consistent with the estimate of DOF in subsection 2.3.

To make a clear comparison of efficiency, Figure 3 gives the log-log plot of the CPU times and corresponding L^2 errors in Table 1. For this special case, the spatial error is the dominant error. Hence, we observe that the former two schemes with sixth-order spatial accuracy are much more efficient than the P^3 SL DG scheme.

Example 3.2 (rigid body rotation). Consider

$$(3.3) \quad u_t - (yu)_x + (xu)_y = 0, \quad x \in [-\pi, \pi], \quad y \in [-\pi, \pi].$$

TABLE 1

(2-D transport equation with constant coefficients). L^2 errors, corresponding order of accuracy, and corresponding CPU times of three different schemes with different meshes and $CFL = 10.2$ for (3.2) with $u(x, y, 0) = \sin(x + y)$ at $T = 2$.

Mesh	SL Hermite			SL hybrid HWENO		
	L^2 error	Order	CPU	L^2 error	Order	CPU
40×40	1.22E-09	—	0.31	1.22E-09	—	0.33
80×80	3.28E-11	5.22	2.39	3.28E-11	5.22	2.58
160×160	5.39E-13	5.93	24.56	5.39E-13	5.93	26.42
320×320	6.93E-15	6.28	305.59	6.93E-15	6.28	318.17
	P^3 SL DG					
40×40	1.07E-07	—	0.58			
80×80	6.84E-09	3.97	4.58			
160×160	3.75E-10	4.19	47.78			
320×320	1.36E-11	4.79	619.95			

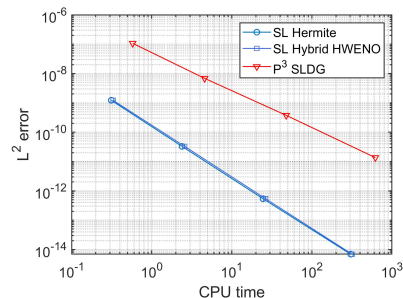


FIG. 3. (2-D transport equation with constant coefficients). A log-log plot of the CPU times and the L^2 errors of three different schemes with meshes of $\{40 \times 40, 80 \times 80, 160 \times 160, 320 \times 320\}$ and $CFL = 10.2$ for (3.2) with $u(x, y, 0) = \sin(x + y)$ at $T = 2$.

We first test (3.3) with a smooth initial data

$$(3.4) \quad u(x, y, 0) = \begin{cases} r_0^b \cos\left(\frac{r^b(\mathbf{x})\pi}{2r_0^b}\right)^6 & \text{if } r^b(\mathbf{x}) < r_0^b, \\ 0 & \text{otherwise,} \end{cases}$$

where $r_0^b = 0.3\pi$, $r^b(\mathbf{x}) = \sqrt{(x - x_0^b)^2 + (y - y_0^b)^2}$, and the center of the cosine bell $(x_0^b, y_0^b) = (0.3\pi, 0)$. In Table 2, we give the L^2 errors, corresponding order of accuracy, and corresponding CPU times of the SL Hermite scheme the SL hybrid HWENO scheme, and the P^3 SL DG scheme with fourth-order splitting method at $T = 2\pi$. The meshes of $\{40 \times 40, 80 \times 80, 160 \times 160, 320 \times 320\}$ are applied. For this case, the splitting error in time dominates the total error. Hence, the orders are fourth for all these schemes. As shown, when the meshes of $\{40 \times 40, 80 \times 80\}$ are applied, the errors of the former two schemes are different. This phenomenon illustrates that the troubled cell indicator misidentifies some cells as troubled cells, especially the cells near extreme points, when the meshes are not dense enough. The misidentification near the extreme points causes the dissipation of the numerical solution because of the adopted HWENO reconstruction. Similar to Example 3.1, Figure 4 shows the log-log plot of the CPU times and corresponding L^2 errors of these three schemes in Table 2. The SL Hermite scheme is observed to be more efficient than the other two schemes.

TABLE 2

(Rigid body rotation). L^2 errors, corresponding order of accuracy, and corresponding CPU times of three different schemes with different meshes and $CFL = 10.2$ for (3.3) with initial condition (3.4) at $T = 2\pi$.

Mesh	SL Hermite			SL hybrid HWENO		
	L^2 error	Order	CPU	L^2 error	Order	CPU
40×40	3.26E-04	—	0.31	9.92E-03	—	0.33
80×80	2.01E-05	4.02	3.55	5.85E-04	4.08	3.81
160×160	1.25E-06	4.01	46.83	1.25E-06	8.87	51.28
320×320	7.83E-08	4.00	662.08	7.83E-08	4.00	669.67
P^3 SL DG						
40×40	3.22E-04	—	0.55			
80×80	2.01E-05	4.00	6.72			
160×160	1.25E-06	4.00	93.02			
320×320	7.83E-08	4.00	1364.52			

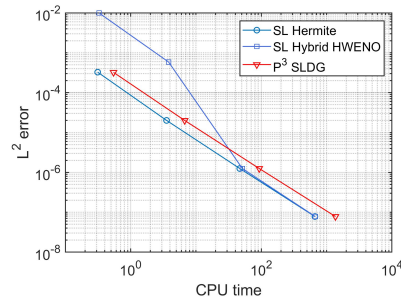


FIG. 4. (Rigid body rotation). A log-log plot of the CPU times and the L^2 errors of three different schemes with meshes of $\{40 \times 40, 80 \times 80, 160 \times 160, 320 \times 320\}$ and $CFL = 10.2$ for (3.3) with initial condition (3.4) at $T = 2\pi$.

Secondly, we solve (3.3) with a discontinuous initial data as shown in Figure 5. The numerical solution of the SL hybrid HWENO scheme with fourth-order splitting at $T = 12\pi$ is shown on the top two panels of Figure 6. Cross-sections of the numerical solution are also provided in Figure 7. We can see that the numerical solution preserves the geometrical morphology of the analytical solution very well. The numerical solution is also positive, nonoscillatory, and of high resolution as observed. On the bottom of Figure 6, we can also observe that the new indicator finds the troubled cell as expected. From Figure 7, which presents two cross-sections of the numerical solution shown in Figure 6, we clearly observe that the numerical solution offers a good approximation of the exact solution.

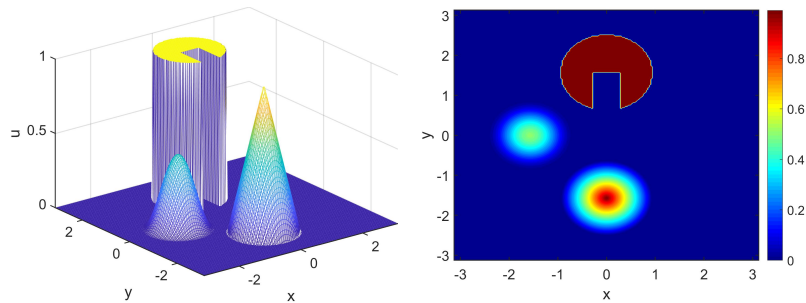


FIG. 5. (Rigid body rotation). The mesh plot (left) and the contour plot (right) of the discontinuous initial data for (3.3).

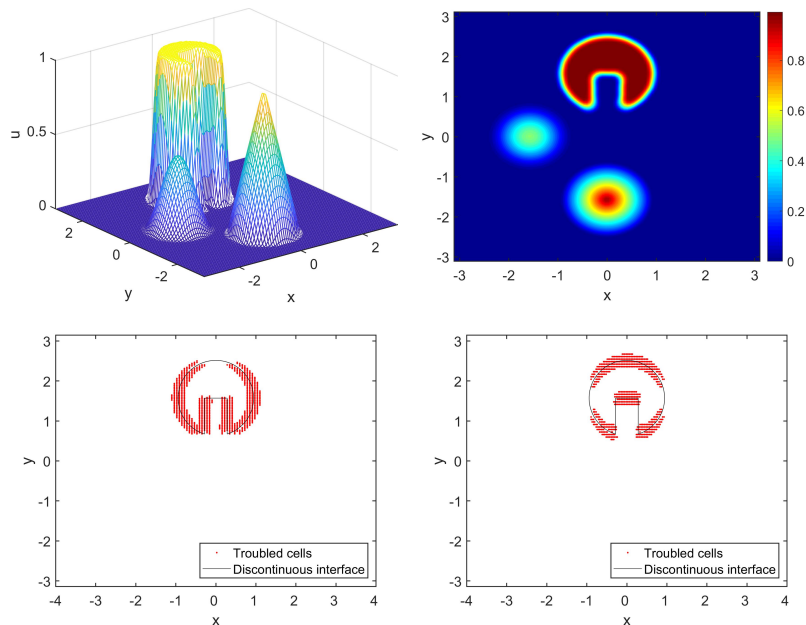


FIG. 6. (Rigid body rotation). Top left and top right panels are the mesh plot and contour plot of the numerical solution of the SL hybrid HWENO scheme with fourth-order splitting for (3.3) with discontinuous initial condition shown in Figure 5 at $T = 12\pi$ with $CFL = 10.2$. Bottom left and bottom right panels are the troubled cells detected by the new indicator at the final time level over x - and y -directions, respectively.

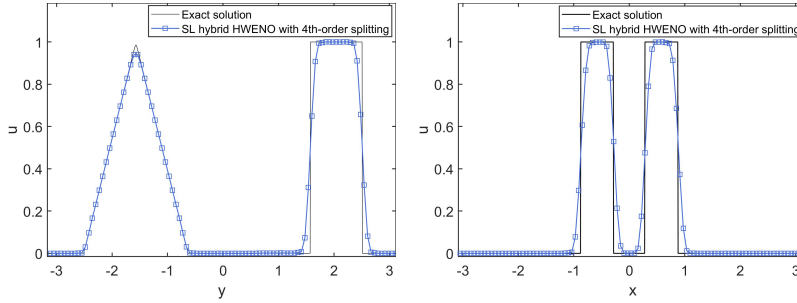


FIG. 7. (Rigid body rotation). Cross-sections at $x = 0$ (left) and $y = 1.2$ (right) of the numerical solution shown in Figure 6.

Example 3.3 (swirling deformation flow). Consider

$$(3.5) \quad u_t - \left(2\pi \cos^2\left(\frac{x}{2}\right) \sin(y) g(t) u \right)_x + \left(2\pi \sin(x) \cos^2\left(\frac{y}{2}\right) g(t) u \right)_y = 0, \\ x \in [-\pi, \pi], \quad y \in [-\pi, \pi],$$

with $g(t) = \cos(\pi t/T)$ and the same initial condition (3.4). Table 3 shows the L^2 errors, corresponding order of accuracy, and corresponding CPU times of the SL Hermite scheme, the SL hybrid HWENO scheme, and the P^3 SL DG scheme with fourth-order splitting method at $T = 1.5$. The meshes of $\{40 \times 40, 80 \times 80, 160 \times 160, 320 \times 320\}$ are applied. We observe that the SL hybrid HWENO scheme has the largest errors. Similarly, the troubled cell indicator misidentifies cells for all the four meshes and causes the loss of accuracy. For the swirling deformation flow, one can check Figure 8 and observe that a smooth bell is deformed to a sharp structure at $t = 0.75$ and the cells near the extreme points are identified as troubled cells. The SL Hermite scheme has the smallest errors for this test as observed, and it takes roughly half the time to compute a result as the P^3 SL DG scheme with the same mesh. Similarly, a log-log plot of the CPU times and corresponding L^2 errors of these three schemes in Table 3 is presented in Figure 9.

To estimate the temporal order of accuracy, we fix a spatial mesh, 160×160 , while varying the CFL number as shown in Figure 10. We can still observe that

TABLE 3

(Swirling deformation flow). L^2 errors, corresponding order of accuracy, and corresponding CPU times of three different schemes with different meshes and $CFL = 10.2$ for (3.5) with initial condition (3.4) at $T = 1.5$.

Mesh	SL Hermite			SL hybrid HWENO		
	L^2 error	Order	CPU	L^2 error	Order	CPU
40×40	4.87E-04	—	0.50	1.52E-02	—	0.47
80×80	1.06E-05	5.52	5.27	1.41E-03	3.43	5.50
160×160	4.12E-08	8.00	71.16	8.09E-06	7.44	73.58
320×320	2.46E-09	4.06	964.05	6.25E-08	7.02	976.25
	P^3 SL DG					
40×40	4.25E-04	—	0.89			
80×80	1.04E-05	5.36	10.31			
160×160	1.23E-07	6.40	146.38			
320×320	5.09E-09	4.60	2044.88			

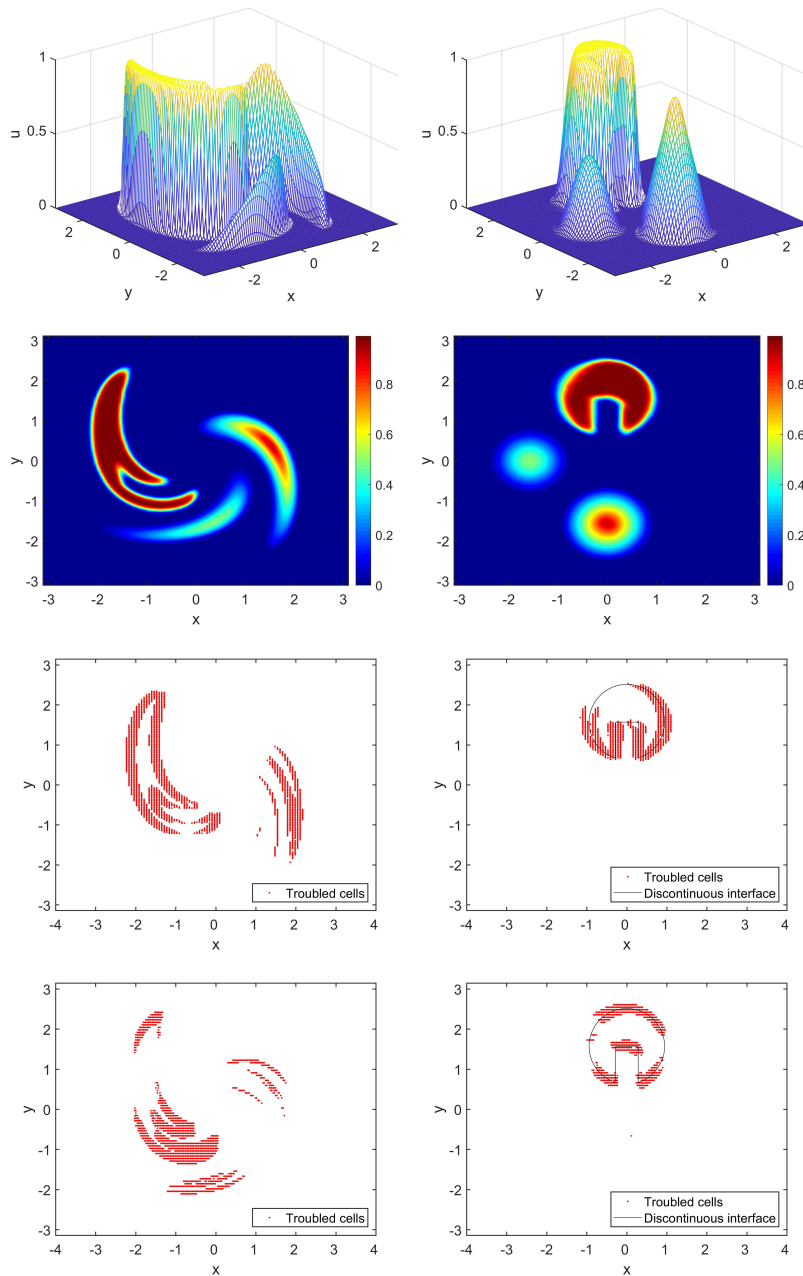


FIG. 8. (Swirling deformation flow). Numerical solutions of the proposed 2-D scheme and troubled cells detected by the new indicator over x - and y -directions at $t = 0.75$ (left) and $t = 1.5$ (right) with $CFL = 10.2$ and a mesh of 100×100 for (3.5) with initial data shown in Figure 5.

the temporal order is at least fourth when the coefficients of (3.5) are dependent of t . We also observe that the error of the SL hybrid HWENO scheme does not go down with refinement of Δt . This is due to the dominant spatial error caused by the misidentification of the troubled cells similar to Table 3 as mentioned above. When the spatial error is dominant, the accumulated error increases with reducing CFL, or

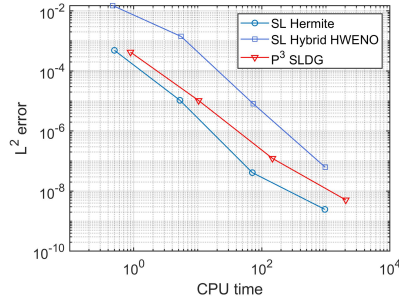


FIG. 9. (*Swirling deformation flow*). A log-log plot of the CPU times and the L^2 errors of three different schemes with meshes of $\{40 \times 40, 80 \times 80, 160 \times 160, 320 \times 320\}$ and $CFL = 10.2$ for (3.5) with initial condition (3.4) at $T = 1.5$.

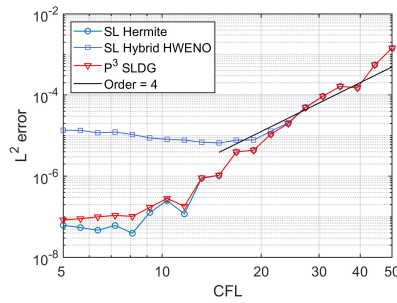


FIG. 10. (*Swirling deformation flow*). Temporal order of accuracy of three different schemes with fourth-order splitting method for (3.5) with initial condition (3.4) at $T = 1.5$. A fixed mesh of 160×160 is used for this test.

Δt , because more time steps are taken. Hence, in Figure 10, the L^2 error slightly goes up for the SL hybrid HWENO scheme (partly for the SL Hermite scheme) as CFL is reduced.

Then, we test (3.5) with the same discontinuous initial condition shown in Figure 5. We numerically evaluate the solution up to $t = 0.75$, when the numerical solution is greatly deformed, and to $T = 1.5$, when the solution is recovered. Numerical solutions at $t = 0.75$ and $t = 1.5$ of the 2-D scheme and the troubled cells detected by the new indicator at the final time with $CFL = 10.2$ are presented in Figure 8. We make the following comments for the results shown in Figure 8:

1. the numerical solution is nonoscillatory and positive as expected;
2. the new troubled cell indicator successfully identifies the troubled cells we need;
3. the third panel on the right side of Figure 8 seems to misidentify some troubled cells. The reason for this is that the numerical solution around those places is smeared so that the indicator detects the cells nearby as good cells.

3.2. Vlasov simulations. In this subsection, we apply the proposed scheme to the 1-D physical space and 1-D velocity space (1D1V) Vlasov–Poisson (VP) system, describing collisionless plasma with a negligible magnetic field, on $(x, v, t) \in \Omega_x \times \mathbb{R} \times \mathbb{R}^+$:

$$(3.6) \quad f_t + v f_x + E(x, t) f_v = 0,$$

$$(3.7) \quad E(x, t) = -\phi_x, \quad -\phi_{xx}(x, t) = \rho(x, t)$$

with periodic boundary condition on the x -dimension and zero boundary condition on the v -dimension. In (3.6) and (3.7), x and v are coordinates in the phase space, $f(x, v, t)$ is the probability distribution function describing the probability of finding a particle at position x with velocity v at time t , E is the electric field, ϕ is the self-consistent electrostatic potential, and $\rho = \int_{\mathbb{R}} f(x, v, t) dv - \rho_0$ is the charge density with $\rho_0 = \frac{1}{|\Omega_x|} \int_{\Omega_x} \int_{\mathbb{R}} f(x, v, 0) dv dx$.

The proposed scheme is a dimensional-splitting-based scheme, which means that it can be easily extended to solve the 1D1V Vlasov–Poisson (VP) system. We use the same framework for this extension as shown in [24, 25] except that we use the fourth-order splitting method. To save space, we briefly describe this extension as follows. Consider the two split subproblem of (3.6):

$$(3.8) \quad f_t + v f_x = 0,$$

$$(3.9) \quad f_t + E(x, t) f_v = 0.$$

Then, the coefficient $E(x, t)$ of (3.9) is reduced to $E^*(x)$ which is obtained by solving the Poisson equation (3.7) based on the solution of the former stage in the splitting procedure. The Poisson equation is solved by a fourth-order local DG (LDG) method [2, 27]. Notice that we can directly obtain $\rho(x_{ig}^i, t) = \sum_{j=1}^{N_v} \frac{h_v}{2} [f(x_{ig}^i, v_1^j, t) + f(x_{ig}^i, v_2^j, t)]$, which is fourth-order accurate at 2 local GL points in each cell, which means that we only have a P^1 nodal DG approximation of ρ for the LDG solver. Hence, we apply a reconstruction in each cell summarized as Algorithm 3.1 to obtain a P^3 nodal DG approximation for the fourth-order LDG solver.

Algorithm 3.1. Reconstruction of ρ on I_i^x .

1. Construct a third-degree Lagrangian interpolation polynomial $\{P_i^\rho(x)\}$ satisfying

$$(3.10) \quad P_i^\rho(x_{ig}^l) = \rho(x_{ig}^l, t), \quad \{l, ig\} \in \{\{i-1, 2\}, \{i, 1\}, \{i, 2\}, \{i+1, 1\}\} := IG^\rho.$$

2. Compute $P_i^\rho(\tilde{x}_{ig}^i)$, where $\{\tilde{x}_{ig}^i\}_{ig=1}^4$ are the 4 local GL points in I_i^x :

$$(3.11) \quad P_i^\rho(\tilde{x}_{ig}^i) = \sum_{\{l, ig\} \in IG^\rho} a_{\{l, ig\}}^{\tilde{ig}} \rho(x_{ig}^l, t), \quad \tilde{ig} = 1, 2, 3, 4,$$

where $\{a_{\{l, ig\}}^{\tilde{ig}}\}$ are constant coefficients independent of i .

Another thing is that we use the SL Hermite scheme instead of the SL hybrid HWENO scheme since the Hermite interpolation has a better capability of capturing the special filamentation structure for the VP system as we observed.

In this subsection, we use the standard tests such as Landau damping, two stream instability, and bump-on-tail instability to verify the effectiveness of the proposed scheme described above for the VP system. In all the tests below, we set the basic numerical parameters as $N_x = 128$, $N_v = 128$, CFL=10.2 and computational domain as $[0, 4\pi] \times [-v_{\max}, v_{\max}]$ with $v_{\max} = 2\pi$ unless otherwise specified, where N_x and N_v are the numbers of cells in the x -direction and v -direction, respectively. We apply the PP limiters for the tests below. The contour figures below are plotted based on nodal values.

Example 3.4 (Landau damping). Consider the VP system with the initial condition

$$(3.12) \quad f(x, v, t = 0) = \frac{1}{\sqrt{2\pi}} (1 + \alpha \cos(kx)) \exp\left(-\frac{v^2}{2}\right),$$

where $k = 0.5$, $\alpha = 0.01$ for the weak Landau damping and $k = 0.5$, $\alpha = 0.5$ for the strong Landau damping. To explain why we use the SL Hermite scheme for the VP system, contour plots of the numerical solutions of the SL hybrid HWENO scheme and SL Hermite scheme with fourth-order splitting for the strong Landau damping at $T = 40$ are provided in Figure 11. We observe that simply using the Hermite interpolation instead of the hybrid HWENO reconstruction gives a better result and the filamentation structure is better captured for the SL Hermite scheme. We also find that the troubled cell indicator misidentifies the cells near the extreme points within those strong filamentation structure as troubled cells, which leads to dissipation as mentioned in the previous subsection. Hence, for all the tests below, we will adopt the SL Hermite scheme with fourth-order splitting.

The time evolutions of the electric field in L^2 norm for both weak and strong Landau dampings are given in Figure 12. For the weak Landau damping, the result reflects the correct damping of the electric field compared with the theoretical value $\gamma = -0.1533$ as plotted with a black solid line in Figure 12. For the strong Landau damping, we find that the initial decay rate is approximately $\gamma_1 = -0.2898$ and the growth rate after $t = 20$ is approximately $\gamma_2 = 0.0825$. Both the decay rate and the growth rate are very close to the existing results in the literature [8, 27].

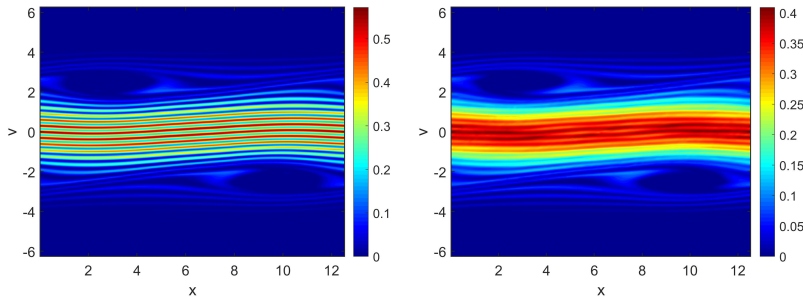


FIG. 11. (Strong Landau damping). Numerical solution of the SL Hermite scheme (left) and SL hybrid HWENO scheme (right) for strong Landau damping at $T = 40$ with $CFL = 10.2$ and a mesh of 128×128 .

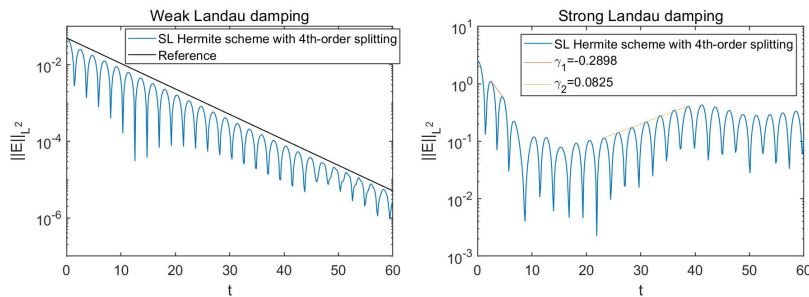


FIG. 12. (Landau damping). Time evolution of the electric field of the SL Hermite scheme for the weak (left) and strong (right) Landau damping with $CFL = 10.2$ and a mesh of 128×128 .

In Figure 13, we present the temporal order of accuracy of the proposed scheme for both weak and strong Landau dampings at $T = 2$ in the same way as the linear tests. The reference solution is computed via taking $\text{CFL} = 0.1$ with a mesh of 160×160 by the proposed scheme. As shown, the temporal order is fourth as expected.

Figure 14 shows the performance of the scheme for preserving mass and L^1 norm for $\alpha = 0.01$ and $\alpha = 0.5$, respectively. The result in Figure 14 takes $v_{\max} = 10$ for revealing the mass conservation property, since the v -dimension is not compact and the zero boundary condition can bring boundary error. As can be seen, the proposed scheme is mass conservative and positive-preserving since the relative deviation is around 10^{-14} and the relative deviation of L^1 norm is completely analogous to the relative deviation of mass by the results in Figure 14. For other kinetic invariants,

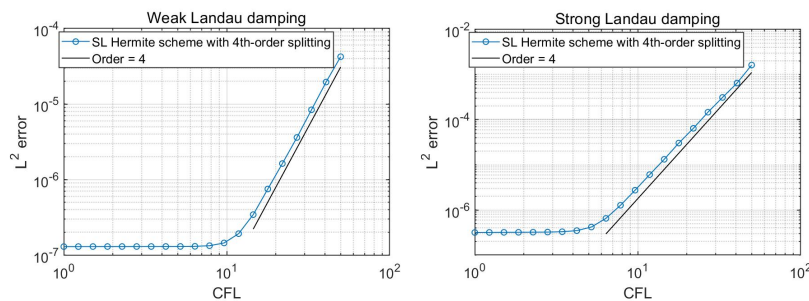


FIG. 13. (Landau damping). Temporal order of accuracy of the SL Hermite scheme for the weak (left) and strong (right) Landau damping at $T = 2$. A fixed mesh of 128×128 is used for this test.

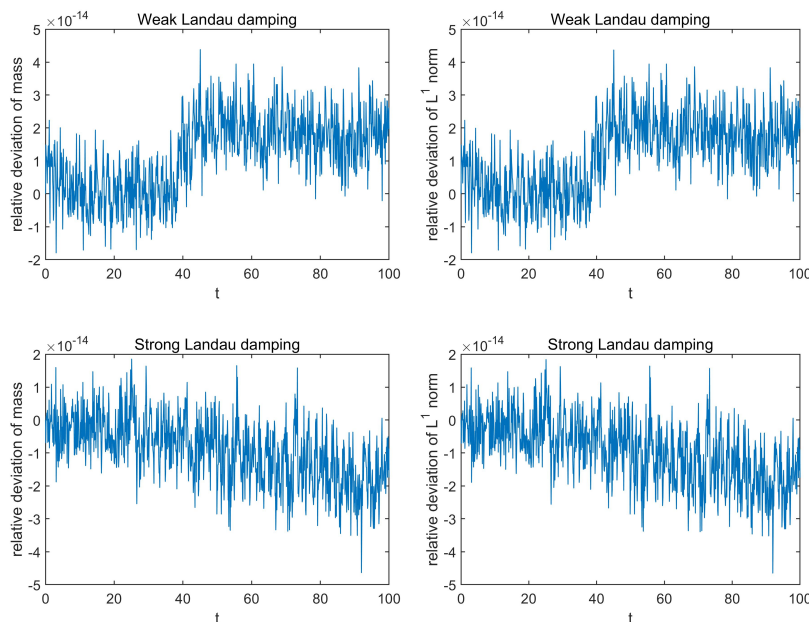


FIG. 14. (Landau damping). Performance of mass conservation and PP properties of the SL Hermite scheme for the weak (top) and strong (bottom) Landau damping.

we observe that the results of preserving the L^2 norm, energy, and entropy are close to the results of those high-order SL schemes [27, 25, 6] in the literature, and we skip these results for space.

Example 3.5 (two stream instability [13]). Consider the symmetric warm two stream instability, i.e., the VP system with the initial condition

$$(3.13) \quad \begin{aligned} f(x, v, t = 0) &= \frac{2}{7\sqrt{2\pi}}(1 + 5v^2) (1 + \alpha ((\cos(2kx) + \cos(3kx)) / 1.2 + \cos(kx))) \exp\left(-\frac{v^2}{2}\right), \end{aligned}$$

where $\alpha = 0.01$ and $k = 0.5$. We present the time evolutions of electric field in L^2 norm for this problem in Figure 15. The result is close to the ones in the literature. On the left of Figure 16, we show the numerical solution of the SL Hermite scheme for the two stream instability at $T = 53$. As is observed, the numerical solution is consistent with the existing ones in the literature [25].

Example 3.6 (bump-on-tail instability [1, 6]). Consider the bump-on-tail instability with the initial condition

$$(3.14) \quad f(x, v, t = 0) = \left(n_p \exp\left(-\frac{v^2}{2}\right) + n_b \exp\left(-\frac{(v-u)^2}{2v_t^2}\right) \right) (1 + 0.04\cos(kx)),$$

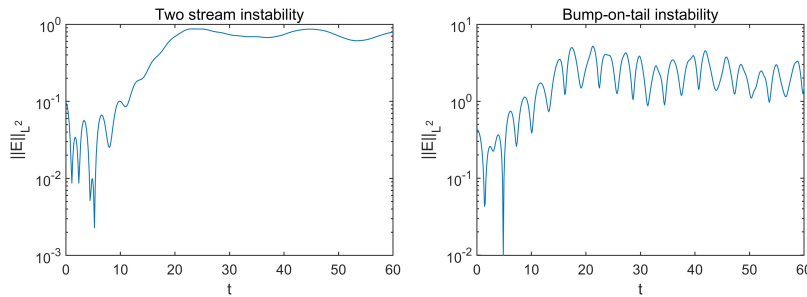


FIG. 15. Time evolution of the electric field of the SL Hermite scheme for the two stream instability (left) and bump-on-tail instability (right) with $CFL = 10.2$ and a mesh of 128×128 .

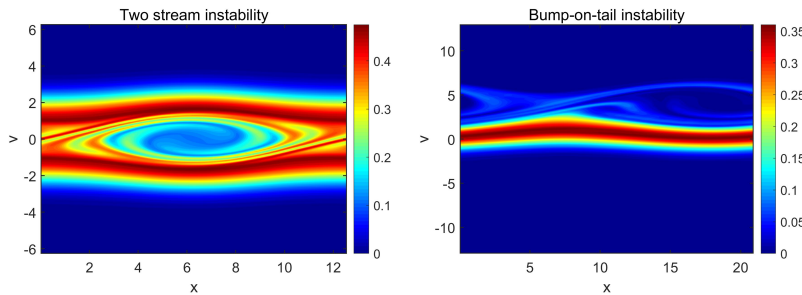


FIG. 16. Numerical solution of the SL Hermite scheme for the two stream instability at $T = 53$ (left) and bump-on-tail instability (right) at $T = 40$ with $CFL = 10.2$ and a mesh of 128×128 .

where $n_p = \frac{9}{10\sqrt{2\pi}}$, $n_b = \frac{2}{10\sqrt{2\pi}}$, $u = 4.5$, $v_t = 0.5$, and $k = 0.3$. The computational domain for this test is $[0, \frac{20}{3}\pi] \times [-13, 13]$ similar to the setting in [6]. Figure 15 gives the time evolution of the electric field of the SL Hermite scheme for the bump-on-tail instability. In Figure 16, we provide the numerical solution of the proposed scheme for bump-on-tail instability at $T = 40$. As shown, the numerical results are consistent with the results in [6].

4. Conclusions. In this paper, we present the SL hybrid HWENO scheme and the SL Hermite scheme for linear transport equations and the nonlinear VP system. The new point of the proposed scheme is that we combine the weak formulation of the characteristic Galerkin method with a hybrid HWENO reconstruction operator or Hermite interpolation operator. This scheme enjoys many good properties including high-order accuracy, nonoscillation, positivity preservation, mass conservation, and high efficiency. Standard models including rigid body rotation, swirling deformation flow, Landau damping, two stream instability, and bump-on-tail instability are tested to verify the properties of the proposed scheme.

Appendix A. Fourth-order dimensional splitting. The fourth-order dimensional splitting for the transport equation (1.1) in the 2-D case can be summarized as follows:

$$(A.1) \quad \begin{aligned} \text{stage 1:} & \text{ evolve } u_t + (au)_x = 0 \text{ for } c_1\Delta t^n, \\ \text{stage 2:} & \text{ evolve } u_t + (bu)_y = 0 \text{ for } d_1\Delta t^n, \\ \text{stage 3:} & \text{ evolve } u_t + (au)_x = 0 \text{ for } c_2\Delta t^n, \\ \text{stage 4:} & \text{ evolve } u_t + (bu)_y = 0 \text{ for } d_2\Delta t^n, \\ \text{stage 5:} & \text{ evolve } u_t + (au)_x = 0 \text{ for } c_3\Delta t^n, \\ \text{stage 6:} & \text{ evolve } u_t + (bu)_y = 0 \text{ for } d_3\Delta t^n, \\ \text{stage 7:} & \text{ evolve } u_t + (au)_x = 0 \text{ for } c_4\Delta t^n, \end{aligned}$$

where the coefficients are defined as follows:

$$(A.2) \quad \begin{aligned} d_1 = d_3 = 1/(2 - 2^{1/3}) &\approx 1.3512, & d_2 = -2^{1/3}/(2 - 2^{1/3}) &\approx -1.7024, \\ c_1 = c_4 = d_1/2 &\approx 0.6756, & c_2 = c_3 = (d_1 + d_2)/2 &\approx -0.1756. \end{aligned}$$

Appendix B. Calculation of the nonlinear weights. For $\{\omega_l\}$, we first calculate the smoothness indicator [21, 18, 29] $\{\beta_l\}$ (we use the same notations as (2.15) for convenience) of $\{q_l(x)\}$. One can refer to [40] for the explicit expression of $\{\beta_l\}$.

Then, similar to (2.16), calculate the parameter τ for $\{\beta_l\}$ above, and the nonlinear weights are defined by

$$(B.1) \quad \omega_l = \frac{\bar{\omega}_l}{\sum_k \bar{\omega}_k} \text{ with } \bar{\omega}_l = \gamma_l \left(1 + \frac{\tau}{\epsilon + \beta_l} \right), \quad l = 1, 2, 3,$$

where $\epsilon = 10^{-6}$.

For $\{\tilde{\omega}_l\}$, the same procedures for calculating $\{\omega_l\}$ are applied based on $\{Q_l(x)\}$. The expression of smoothness indicators $\{\tilde{\beta}_l\}$ for $\{Q_l(x)\}$ can be found in [3].

Appendix C. Proof of Proposition 2.3.

Proof. Consider the linear transport equation (2.1) with constant coefficient, $a(x, t) \equiv a$, and periodic boundary condition. Without loss of generality, we as-

sume that $a > 0$ and that CFL is less than 1. When CFL is greater than 1, the linear scheme could always be reduced to a whole solution shifting on a uniform mesh together with the scheme having CFL less than 1.

The numerical update given by the SL Hermite scheme is then summarized as

$$\begin{aligned}
 \text{(C.1)} \quad \bar{u}_j^{n+1} &= \frac{1}{h} \int_{x_{j-1/2} - (1-\nu)h}^{x_{j-1/2}} \mathcal{H}_{j-1}(\bar{u}_{j-2}^n, \bar{u}_{j-1}^n, \bar{u}_j^n, \bar{v}_{j-2}^n, \bar{v}_{j-1}^n, \bar{v}_j^n) dx \\
 &\quad + \frac{1}{h} \int_{x_{j-1/2}}^{x_{j-1/2} + \nu h} \mathcal{H}_j(\bar{u}_{j-1}^n, \bar{u}_j^n, \bar{u}_{j+1}^n, \bar{v}_{j-1}^n, \bar{v}_j^n, \bar{v}_{j+1}^n) dx, \\
 \bar{v}_j^{n+1} &= \frac{1}{h} \int_{x_{j-1/2} - (1-\nu)h}^{x_{j-1/2}} \mathcal{H}_{j-1}(\bar{u}_{j-2}^n, \bar{u}_{j-1}^n, \bar{u}_j^n, \bar{v}_{j-2}^n, \bar{v}_{j-1}^n, \bar{v}_j^n) \left(\frac{x + (1-\nu)h - x_j}{h} \right) dx \\
 &\quad + \frac{1}{h} \int_{x_{j-1/2}}^{x_{j-1/2} + \nu h} \mathcal{H}_j(\bar{u}_{j-1}^n, \bar{u}_j^n, \bar{u}_{j+1}^n, \bar{v}_{j-1}^n, \bar{v}_j^n, \bar{v}_{j+1}^n) \left(\frac{x + (1-\nu)h - x_j}{h} \right) dx \quad \forall j,
 \end{aligned}$$

where $\nu = 1 - a\Delta t^n/h$.

We prove the proposition via von Neumann stability analysis by assuming

$$\text{(C.2)} \quad \bar{u}_l^n = \bar{u}^n e^{I\xi lh}, \quad \bar{v}_l^n = \bar{v}^n e^{I\xi lh} \quad \text{for } l = j - 2, j - 1, j, j + 1$$

and

$$\text{(C.3)} \quad \bar{u}_j^{n+1} = \bar{u}^{n+1} e^{I\xi jh}, \quad \bar{v}_j^{n+1} = \bar{v}^{n+1} e^{I\xi jh},$$

where I is the imaginary unit. Substituting (C.2) and (C.3) into (C.1), we obtain

$$\text{(C.4)} \quad \begin{bmatrix} \bar{u}^{n+1} \\ \bar{v}^{n+1} \end{bmatrix} = A(\nu, \xi) \begin{bmatrix} \bar{u}^n \\ \bar{v}^n \end{bmatrix}, \quad \square$$

where $A(\nu, \xi)$ is the 2×2 amplification matrix. We skip the explicit expression of $A(\nu, \xi)$ for brevity and denote the spectral radius of $A(\nu, \xi)$ by $\rho(A(\nu, \xi))$. For numerical stability, it is sufficient to show that $\rho(A(\nu, \xi)) \leq 1$ for any $\nu \in [0, 1]$ and $\xi h \in [0, 2\pi]$. We numerically check the spectral radius by sampling 1000 uniform points in the ν and ξ domains, respectively. As can be seen in Figure 17, all the values $\rho(A(\nu, \xi)) - 1$ do not exceed 0, which validates Proposition 2.3.

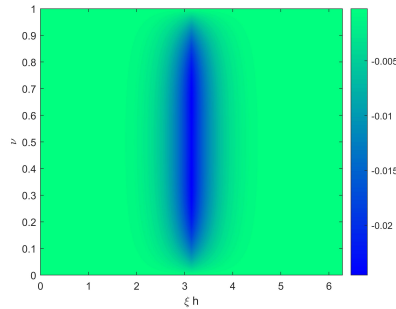


FIG. 17. Numerical plot of $\rho(A(\nu, \xi)) - 1$ for all sampling points.

Appendix D. PP limiters for Algorithms 2.1 and 2.2. The PP limiter applied on Algorithm 2.1 is shown in Algorithm D.1.

Algorithm D.1. PP limiter for Algorithm 2.1 for given y_{jg}^j and i (pseudo code).

```

1: if  $\bar{u}_i^{j,jg} < 0$ 
2:    $ex = 0$ ;  $accum = \bar{u}_i^{j,jg}$ ;
3:   while ( $accum < 0$ )
4:      $ex = ex + 1$ ;
5:      $accum = accum + \bar{u}_{i-ex}^{j,jg} + \bar{u}_{i+ex}^{j,jg}$ ;
6:   end
7:    $accum = accum / (1 + 2ex)$ ;
8:    $\theta = \min\{|accum/(\bar{u}_i^{j,jg} - accum)|, 1\}$ ;
9:    $\bar{u}_{i-ex:i+ex}^{j,jg} = \theta(\bar{u}_{i-ex:i+ex}^{j,jg} - accum) + accum$ ;
10: end

```

For convenience, we define a new array $\{x(k)\}$ such that $x(2i - 1) = x_1^i$ and $x(2i) = x_2^i$. The PP limiter applied on Algorithm 2.2 is presented in Algorithm D.2.

Algorithm D.2. PP limiter for Algorithm 2.2 for given y_{jg}^j and i (pseudo code).

```

1: if  $H_i(x(2i - 1)) < 0$ 
2:    $ex = 0$ ;  $accum = H_i(x(2i - 1))$ ;
3:   while ( $accum < 0$ )
4:      $ex = ex + 1$ ;
5:      $accum = accum + H_i(x(2i - 1 - ex)) + H_i(x(2i - 1 + ex))$ ;
6:   end
7:    $accum = accum / (1 + 2ex)$ ;
8:    $\theta = \min\{|accum/(H_i(x(2i - 1)) - accum)|, 1\}$ ;
9:    $H_i(x(2i - 1 - ex : 2i - 1 + ex)) = \theta(H_i(x(2i - 1 - ex : 2i - 1 + ex)) - accum)$ 
    $+ accum$ ;
10: end
11: if  $H_i(x(2i)) < 0$ 
12:    $ex = 0$ ;  $accum = H_i(x(2i))$ ;
13:   while ( $accum < 0$ )
14:      $ex = ex + 1$ ;
15:      $accum = accum + H_i(x(2i - ex)) + H_i(x(2i + ex))$ ;
16:   end
17:    $accum = accum / (1 + 2ex)$ ;
18:    $\theta = \min\{|accum/(H_i(x(2i)) - accum)|, 1\}$ ;
19:    $H_i(x(2i - ex : 2i + ex)) = \theta(H_i(x(2i - ex : 2i + ex)) - accum) + accum$ ;
20: end

```

REFERENCES

- [1] T. ARBER AND R. VANN, *A critical comparison of Eulerian-grid-based Vlasov solvers*, J. Comput. Phys., 180 (2002), pp. 339–357.
- [2] D. N. ARNOLD, F. BREZZI, B. COCKBURN, AND L. D. MARINI, *Unified analysis of discontinuous Galerkin methods for elliptic problems*, SIAM J. Numer. Anal., 39 (2002), pp. 1749–1779.

- [3] D. S. BALSARA, S. K. GARAIN, AND C. SHU, *An efficient class of WENO schemes with adaptive order*, J. Comput. Phys., 326 (2016), pp. 780–804.
- [4] P. A. BOSLER, A. M. BRADLEY, AND M. A. TAYLOR, *Conservative multimoment transport along characteristics for discontinuous Galerkin methods*, SIAM J. Sci. Comput., 41 (2019), pp. B870–B902.
- [5] A. BURBEAU AND P. SAGAUT, *A dynamic p -adaptive discontinuous Galerkin method for viscous flow with shocks*, Comput. & Fluids, 34 (2005), pp. 401–417.
- [6] X. CAI, W. GUO, AND J.-M. QIU, *A high order semi-Lagrangian discontinuous Galerkin method for Vlasov-Poisson simulations without operator splitting*, J. Comput. Phys., 354 (2018), pp. 529–551.
- [7] X. CAI, X. ZHANG, AND J. QIU, *Positivity-preserving high order finite volume HWENO schemes for compressible Euler equations*, J. Sci. Comput., 68 (2016), pp. 464–483.
- [8] C.-Z. CHENG AND G. KNORR, *The integration of the Vlasov equation in configuration space*, J. Comput. Phys., 22 (1976), pp. 330–351.
- [9] N. CROUSEILLES, M. MEHRENBARGER, AND F. VECIL, *Discontinuous Galerkin semi-Lagrangian method for Vlasov-Poisson*, ESAIM Proc., 32 (2011), pp. 211–230.
- [10] H. K. DAHLE, R. E. EWING, AND T. F. RUSSELL, *Eulerian-Lagrangian localized adjoint methods for a nonlinear advection-diffusion equation*, Comput. Methods Appl. Mech. Engrg., 122 (1995), pp. 223–250.
- [11] M. DUMBSER, D. S. BALSARA, E. F. TORO, AND C.-D. MUNZ, *A unified framework for the construction of one-step finite volume and discontinuous Galerkin schemes on unstructured meshes*, J. Comput. Phys., 227 (2008), pp. 8209–8253.
- [12] L. EINKEMMER, *A performance comparison of semi-Lagrangian discontinuous Galerkin and spline based Vlasov solvers in four dimensions*, J. Comput. Phys., 376 (2019), pp. 937–951.
- [13] F. FILBET AND E. SONNENDRÜCKER, *Comparison of Eulerian Vlasov solvers*, Comput. Phys. Commun., 150 (2003), pp. 247–266.
- [14] E. FOREST AND R. D. RUTH, *Fourth-order symplectic integration*, Phys. D, 43 (1990), pp. 105–117.
- [15] W. GUO, R. D. NAIR, AND J. M. QIU, *A conservative semi-Lagrangian discontinuous Galerkin scheme on the cubed sphere*, Monthly Weather Rev., 142 (2014), pp. 457–475.
- [16] C. HUANG, T. ARBOGAST, AND J. QIU, *An Eulerian-Lagrangian WENO finite volume scheme for advection problems*, J. Comput. Phys., 231 (2012), pp. 4028–4052.
- [17] C.-S. HUANG, T. ARBOGAST, AND C.-H. HUNG, *A semi-Lagrangian finite difference WENO scheme for scalar nonlinear conservation laws*, J. Comput. Phys., 322 (2016), pp. 559–585.
- [18] G.-S. JIANG AND C.-W. SHU, *Efficient implementation of weighted ENO schemes*, J. Comput. Phys., 126 (1996), pp. 202–228.
- [19] D. KUZMIN, *A vertex-based hierarchical slope limiter for p -adaptive discontinuous Galerkin methods*, J. Comput. Appl. Math., 233 (2010), pp. 3077–3085.
- [20] D. LEE, R. B. LOWRIE, M. R. PETERSEN, T. D. RINGLER, AND M. W. HECHT, *A high order characteristic discontinuous Galerkin scheme for advection on unstructured meshes*, J. Comput. Phys., 324 (2016), pp. 289–302.
- [21] X.-D. LIU, S. OSHER, AND T. CHAN, *Weighted essentially non-oscillatory schemes*, J. Comput. Phys., 115 (1994), pp. 200–212.
- [22] K. W. MORTON, *On the analysis of finite volume methods for evolutionary problems*, SIAM J. Numer. Anal., 35 (1998), pp. 2195–2222.
- [23] J. QIU AND C.-W. SHU, *Hermite WENO schemes and their application as limiters for Runge-Kutta discontinuous Galerkin method: One-dimensional case*, J. Comput. Phys., 193 (2004), pp. 115–135.
- [24] J.-M. QIU AND A. CHRISTLIEB, *A conservative high order semi-Lagrangian WENO method for the Vlasov equation*, J. Comput. Phys., 229 (2010), pp. 1130–1149.
- [25] J.-M. QIU AND C. W. SHU, *Positivity preserving semi-Lagrangian discontinuous Galerkin formulation: Theoretical analysis and application to the Vlasov-Poisson system*, J. Comput. Phys., 230 (2011), pp. 8386–8409.
- [26] M. RESTELLI, L. BONAVENTURA, AND R. SACCO, *A semi-Lagrangian discontinuous Galerkin method for scalar advection by incompressible flows*, J. Comput. Phys., 216 (2006), pp. 195–215.
- [27] J. A. ROSSMANITH AND D. C. SEAL, *A positivity-preserving high-order semi-Lagrangian discontinuous Galerkin scheme for the Vlasov-Poisson equations*, J. Comput. Phys., 230 (2011), pp. 6203–6232.
- [28] T. F. RUSSELL AND M. A. CELIA, *An overview of research on Eulerian-Lagrangian localized adjoint methods (ELLAM)*, Adv. Water Res., 25 (2002), pp. 1215–1231.

- [29] C.-W. SHU, *Essentially non-oscillatory and weighted essentially non-oscillatory schemes for hyperbolic conservation laws*, in *Advanced Numerical Approximation of Nonlinear Hyperbolic Equations*, Springer, Cham, 1998, pp. 325–432.
- [30] Z. TAO, F. LI, AND J. QIU, *High-order central Hermite WENO schemes: Dimension-by-dimension moment-based reconstructions*, *J. Comput. Phys.*, 318 (2016), pp. 222–251.
- [31] L. WANG AND D. J. MAVRIPLIS, *Adjoint-based h - p adaptive discontinuous Galerkin methods for the 2D compressible Euler equations*, *J. Comput. Phys.*, 228 (2009), pp. 7643–7661.
- [32] T. XIONG, J.-M. QIU, Z. XU, AND A. CHRISTLIEB, *High order maximum principle preserving semi-Lagrangian finite difference WENO schemes for the Vlasov equation*, *J. Comput. Phys.*, 273 (2014), pp. 618–639.
- [33] H. YOSHIDA, *Construction of higher order symplectic integrators*, *Phys. Lett. A*, 150 (1990), pp. 262–268.
- [34] H. YOSHIDA, *Recent progress in the theory and application of symplectic integrators*, in *Qualitative and Quantitative Behaviour of Planetary Systems*, Springer, Cham, 1993, pp. 27–43.
- [35] X. ZHANG AND C. W. SHU, *On maximum-principle-satisfying high order schemes for scalar conservation laws*, *J. Comput. Phys.*, 229 (2010), pp. 3091–3120.
- [36] X. ZHANG AND C. W. SHU, *On positivity-preserving high order discontinuous Galerkin schemes for compressible Euler equations on rectangular meshes*, *J. Comput. Phys.*, 229 (2010), pp. 8918–8934.
- [37] X. ZHANG AND C.-W. SHU, *Maximum-principle-satisfying and positivity-preserving high-order schemes for conservation laws: Survey and new developments*, *Proc. A*, 467 (2011), pp. 2752–2776.
- [38] Y. ZHANG AND R. NAIR, *A nonoscillatory discontinuous Galerkin transport scheme on the cubed sphere*, *Monthly Weather Rev.*, 140 (2012), pp. 3106–3126.
- [39] Z. ZHAO, Y. CHEN, AND J. QIU, *A hybrid Hermite WENO scheme for hyperbolic conservation laws*, *J. Comput. Phys.*, 405 (2020), 109175.
- [40] Z. ZHAO AND J. QIU, *A Hermite WENO scheme with artificial linear weights for hyperbolic conservation laws*, *J. Comput. Phys.*, 417, 109583.
- [41] J. ZHU AND J. QIU, *A new fifth order finite difference WENO scheme for solving hyperbolic conservation laws*, *J. Comput. Phys.*, 318 (2016), pp. 110–121.